14th Int. Conference on Solid State Lighting and LED-based Illumination Systems, San Diego, CA; Aug 12-13, 2015
Proc. SPIE 9571, Paper 95710P, (Sept. 08, 2015); http://dx.doi.org/10.1117/12.2188612

Optoelectronic and structural properties of InGaN grown by Migration-Enhanced, Plasma-Assisted MOCVD

Daniel Seidlitz[a,b], M.K.I. Senevirathna[a], Y. Abate[a], A. Hoffmann[b] and N. Dietz[a,*]

[a] Dept. Physics & Astronomy; Center for Nano Optics, Georgia State University (GSU), Atlanta, GA 30303
[b] Institute of Solid State Physics, Technical University (TU) Berlin, Berlin, Germany

ABSTRACT

We present optoelectronic and structural layer properties of InN and InGaN epilayers grown on sapphire templates by Migration-Enhanced Plasma Assisted Metal Organic Chemical Vapor Deposition (MEPA-MOCVD). Real-time characterizations have been conducted during the growth process to gain insight of the plasma-assisted decomposition of the nitrogen precursor and associated growth surface processes. Analyzed Plasma Emission Spectroscopy (PES) and UV Absorption Spectroscopy (UVAS) provide detection and concentrations of plasma generated active species (N*/NH*/NHx*). Various precursors have been used to assess the nitrogen-active fragments that are directed from the hollow cathode plasma tube to the growth surface. The in-situ diagnostics results are supplemented with ex-situ materials structures investigation results of nanoscale structures using high-resolution scattering type Scanning Near-field Optical Microscopy (s-SNOM). The structural properties have been analyzed by Raman spectroscopy and Fourier transform infrared (FTIR) reflectance. The Optoelectronic and optical properties were extracted by modeling the FTIR reflectance (e.g. free carrier concentration, high frequency dielectric constant, mobility) and optical absorption spectroscopy. The correlation and comparison between the in-situ metrology results with the ex-situ nano-structural and optoelectronic layer properties provides insight into the growth mechanism on how plasma-activated nitrogen-fragments can be utilized as nitrogen precursor for group III-nitride growth. The here assessed growth process parameter focus on the temporal precursor exposure of the growth surface, the reactor pressure, substrate temperature and their effects of the properties of the InN and InGaN epilayers.

Keywords: InN, InGaN, migration-enhanced plasmas-assisted MOCVD, epitaxial growth, FTIR, layer thickness, Raman, Reflectance

1. INTRODUCTION

The growth of high-quality indium-rich ternary/multinary group III-nitrides (III-Ns') and heterostructures and nano-structured alloys (QWs', QDs', etc.) thereof are highly sought for the realization of frequency agile optical devices, and high-power, high-frequency optoelectronic device structures. A crucial element in the realization of such devices is the integration of indium-rich III-Ns' into wide bandgap III-N materials (e.g. Ga-/Al-rich III-Ns'), enabling device structures based on the high electron mobility in indium-rich alloys. InN in particular, is highly attractive due to its small effective mass and one of the highest mobility of electrons (500 - 4000 cm2/Vs)[1,2], high saturation velocity[3] and smallest band gap of about 0.7eV[4] in the AlN-GaN-InN nitride family.

Even though significant progress has been made in recent years, in the stabilization and growth of InN and indium-rich InGaN epilayers by low-pressure MOCVD[5] and plasma-assisted MBE techniques[6-8], the structural quality both in macro- and nano-meter spatial scales and the integration into wide band-gap III-Ns' is still a challenge due to the large growth temperature differences between the group III-N binaries. The still highly conflicting reports on the basic physical properties of InN[9] and indium-rich group III-N alloys, depending on the growth technique used, indicate that further studies on the growth chemistry of indium-rich III-Ns' with different approaches on the stabilization of indium-rich InGaN alloys are needed to understand the fundamental properties of indium-rich III-Ns'. In particular, studies on the relationships between the growth temperature, surface stabilization, group III precursor surface fragments, with resulting point defects in the incorporated layer may foster a more detailed understanding of the microstructure of InGaN growth chemistry[10]. In particular utilization of state of the art near-field and far-field optical spectroscopic tools that proved high spatial resolution, way below the diffraction limit (for example s-SNOM offers typical resolution of ~15 nm), will play a critical role in understanding the fundamental physical and structural properties correlated with growth parameters.

*ndietz@gsu.edu; phone (404) 413-6002; www.physics.gsu.edu/dietz

For the integration of indium-rich InGaN epilayers into wide-band III-Ns' (e.g. aluminum- or gallium-rich III-Ns') alloys, a significant reduction of the growth temperature gaps between the binaries will be required – either by thermodynamics- or kinetics means in order to stabilize not only the growth surface, but also to prevent the decomposition of any underlying indium-rich III-N layer grown at lower temperatures. These growth techniques are motivated by the same intent to stabilize the growth surface by either thermodynamic or by kinetics means, both controlling the sensitive relationship between the properties of compounds and their native defect chemistry.

The thermodynamic controlled growth at superatmospheric reactor pressures has shown that the native defect density depends on the control of compound stoichiometry, that is, on the partial pressure of volatile constituents in thermal equilibrium.

A thermodynamic approach to stabilize indium-rich InGaN structures at higher growth temperatures and narrow the gap of growth temperature of group III nitride epilayers, has been explored by superatmospheric MOCVD[11-13]. As depicted in Fig. 1(a), we demonstrated that InN and indium-rich InGaN epilayer can be stabilized indeed at significant much higher growth temperatures as a function of super-atmospheric reactor pressures, reducing the temperature gap between the binaries InN and GaN. A further advantage discovered was the higher cracking efficiency of the utilized ammonia precursor, enabling a lower group V/III precursor ratio during the growth. However, as shown in Fig. 1(b), a significant drawback is the reduced growth rate at higher reactor pressures due to the smaller diffusion length at higher pressures for a given fixed reactor height. An advance reactor configuration with a reactor flow channel height adjustment configuration might overcome this limitation.

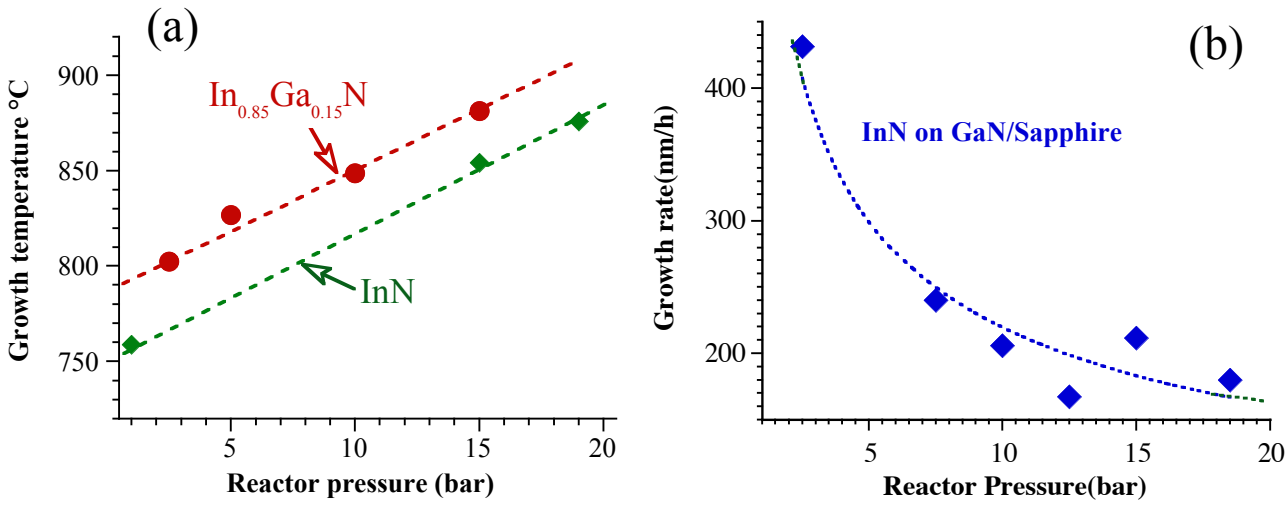

Fig. 1: (a) Growth temperature versus reactor pressure for the growth of InGaN epilayers under superatmospheric MOCVD growth conditions, **(b)** decrease of growth rate with increasing reactor pressure for a fixed reactor flow channel height.

In this contribution, we explore to narrow the growth temperature gaps between the III-N's binaries by kinetic means, using the kinetic energies of ionized nitrogen fragments in the afterglow plasma regime to stabilize the growth surface as well as group V-precursor fragments.

Recent advances in the hollow cathode plasma source development and their utilization in MEP-MOCVD growth of InGaN epilayers indicate that the kinetic stabilization of the growth surface is an equivalent, viable approach, with potential additional degrees of freedom in the process parameter space to further stabilize the growth surface.

2. EXPERIMENTAL

For the growth of group III-N heterostructures and nanostructured alloys, a customized MEPA-MOCVD reactor has been utilized as depicted in Fig. 2a. The reactor has an attached load-lock system and accommodates up to Ø 4" substrates (or 3 × Ø 2" substrates), which can be heated to above 1100 °C. The reactor base pressure is below 10^{-8} mbar (via turbo molecular pump and roughing pump station) with a reactor growth pressure operation range from 1 mbar to 10

mbar. A customized showerhead injection system accommodates the temporal and spatially controlled injection of MO sources (e.g., Trimethylindium (TMI), Trimethylgallium (TMG), Trimethylaluminum (TMA), etc.). As nitrogen precursor, a Meaglow oxygen-free hollow-cathode[14] nitrogen (N_2) plasma source with downstream added hydride precursors (e.g. H_2, NH_3, SiH_4, GeH_4, etc.) is utilized for the generation of $N_2^*/NH^*/NH_x^*$ fragments and adduct thereof with tailored kinetic energies provided via a 600W (13.56 MHz) rf-power source. The plasma afterglow region above the growth surface can be adjusted via a bias voltage. The plasma fragments within the plasma and the afterglow region are monitored by plasma emission (PE) spectroscopy - as illustrated in Fig. 2a - in the wavelength region of 200 nm to 1000 nm. The epitaxial deposition process for InGaN was carried out with a precursor supply mode as illustrated in Fig. 2b, varying plasma and MO exposures, precursor separation times, reactor pressure, growth temperature, and plasma power. The group V/III molar precursor ratio is controlled indirectly through the rf-power with a constant N_2 flow of 750 sccm through the hollow-cathode tube, and the bias of the ion-stream. The MO pulse width was kept constant at 1 sec with a flow rates of 9.6 µmol/min and 11 for TMI and TMG, respectively. For InGaN growth, the TMI and TMG flows were adjusted such that the to targeted TMI:TMG ratio and MO surface coverage per cycle sequence are achieved. The N-precursor pulse width and rf-power amplitude were varied as described in the result sections below.

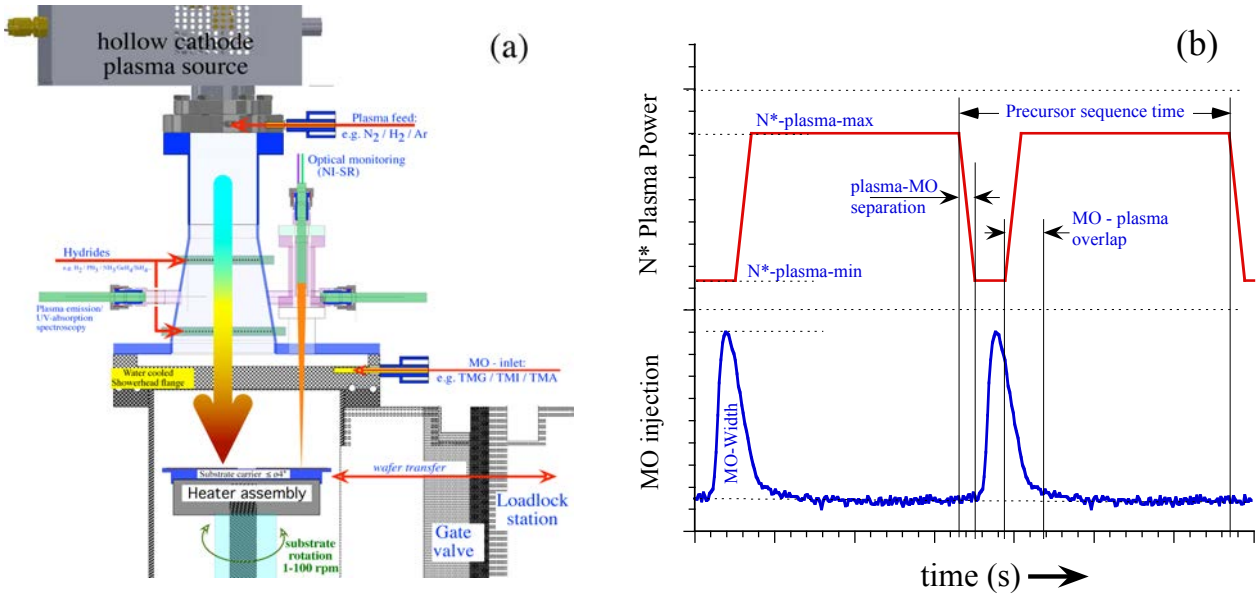

Fig. 2: (a) Custom build MEPA-MOCVD growth system with load lock, ⌀ 4.5" substrate carrier, and Meaglow Hollow cathode plasma source; **(b)** Schematics of temporal and spatial TMG and N*-plasma precursor injection modulation.

The properties of the InGaN layers where assessed by Raman, Fourier transform infrared (FTIR) and normal-incidence reflectance (NIR) spectroscopy. Raman spectroscopy was applied to analyze the bonding and local ordering of the InN epilayers. The customized Raman spectrometer uses a liquid N_2-cooled multichannel charge-coupled (CCD) camera with a single 2m-monochromator system to record the inelastic Raman scattering. The Raman measurements were carried out in backscattering geometry along the [0001] crystal orientation, using an excitation energy of 2.33 eV at room temperature.

For FTIR spectroscopy, a Perkin-Elmer 2000 system was utilized. The FTIR reflection measurements were performed at room temperature on a Perkin-Elmer Fourier-transform infrared spectrometer with an HgCdTe (MCT) detector and KBr beam-splitter for the range of 400-7000cm^{-1} (0.04965 to 0.8068 eV) under the near-normal incidence geometry (less than 8^o incidence angle). The IR reflectance spectra were analyzed using a multilayer stack model and a Lorentz-Drude model for the far- and mid-IR spectral regime and determine the phonon frequencies, effective dielectric function e_∞, plasma frequency, layer thickness, and damping parameters, from which the free carrier concentration and carrier mobility for each layer can be calculated[15,16]. NIR spectroscopic measurements were carried out from 200 nm to 1100 nm using a Deuterium/Halogen light source, a StellarNet SILVER-Nova spectrometer with a TE-cooled linear CCD array, and corrective optics. The reflectance spectra where analyzed using multilayer stack structures and model dielectric functions for each layer in order to obtain layer thickness and optical properties for the deposited InGaN layers[17].

3. RESULTS AND DISCUSSION

3.1. Hollow-Cathode plasma characterization and GaN growth with N*-plasma / ammonia (NH_3) by-mix

Using an oxygen-free Meaglow hollow cathode plasma as the nitrogen precursor source for the growth of group III-nitride alloys provides a challenge to correlate the nitrogen flow through the hollow-cathode and the rf-power supplied to the hollow cathode to a number density and the kinetic energies of reactive nitrogen fragment reaching the growth surface. The active nitrogen precursor density in the afterglow plasma region above the surface is therefore a convoluted function on rf-power, nitrogen flow through the hollow cathode, gas density (e.g reactor pressure), by-mixed hydrides (e.g. H_2, NH_3, etc.), bias of ions and distance to the growth surface. Of specific interest are the constituents in the afterglow plasma region, their kinetic energies and their spatial and temporal distributions, which enables to tailoring of the surface chemistry processes and the stabilization of the growth surface. Fig. 3a shows an image of the afterglow plasma region after it passed an electric grid.

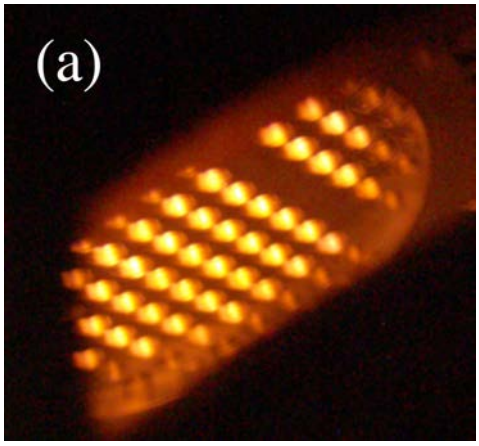

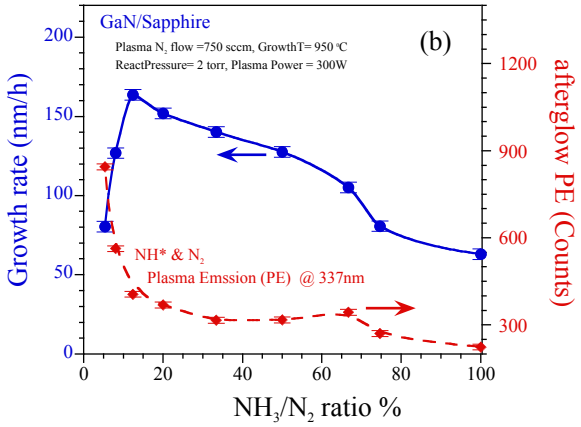

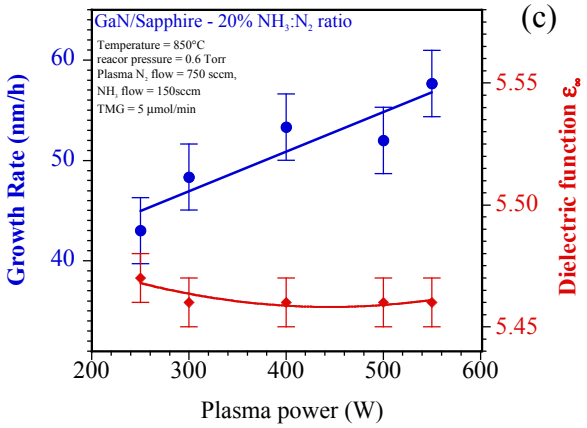

Fig. 3:

(a) Hollow Cathode N*-plasma afterglow regime monitored ½" above growth surface with source biasing;

(b) Correlation of GaN growth rates with PE emission of NH* and N2* emission at λ=337nm and ammonia by-mixing in plasma stream (see text);

(c) GaN growth rates with increasing N*-plasma power and 20% NH3 by-mix in plasma stream.

The active nitrogen-containing species (e.g. N^* / NH_x^*, …) and their energies are controlled by the flow of species through the hollow cathode (typ. N_2), the rf-power supplied to the hollow cathode (typ. 150W – 600W) and the by-mixing the hydride sources (e.g. NH_3 / H_2) into the plasma stream. At this point, only little is known how these parameters relate to the type of species reaching the growth surface, their kinetic energies they are carrying, their life time, their effect on stabilization of the growth surface, and/or their reactivity with the MO-precursor fragments, and so forth. To explore some of the parameter, we looked at the effect of ammonia by-mixing into the N-plasma stream and how it affects the growth and layer properties of GaN. As shown in Fig. 3b, the growth rate of GaN sharply increases with NH_3 by-mix of about 20% and steadily decreases. At the same time, the plasma emission (PE) line in the afterglow region at 337nm (associated with NH^* & N_2 species) decreases rapidly with increased NH_3 by-mix, indicating that small amount of NH_x^* species (< 20%) enhances the growth relevant nitrogen species at the growth surface, while larger amounts quenches active nitrogen-containing species. Further systematic studies are needed to understand the plasma-assisted gas phase chemistry involving nitrogen and hydride containing species. Here, the influence of the rf-power on the GaN growth rate and effective dielectric function (DF) e_∞, is depicted in Fig. 3c, for nitrogen plasma stream

containing 20% NH_3. With increase of plasma power the growth rate increases and e_∞ stabilizes. The GaN surfaces are smooth with root mean square (RMS) values below 2 nm, which slightly increases with plasma power.

3.2. Influence of reactor pressure and growth temperature on InN properties

To establish an initial processing window for InN, we first assessed the reactor pressure and growth temperature window. As show in Fig. 4 (a) and (b), the local structural quality – as assess by the Raman E_2(high) mode – indicate an optimum around 3 torr, even though the growth rate increase further with increased reactor pressures as depicted in Fig. 4(b). The substrate growth temperature window was assessed from 550°C up to 800°C, using a 14 sec pulsed Plasma exposure and 1 sec TMI pulse exposure.

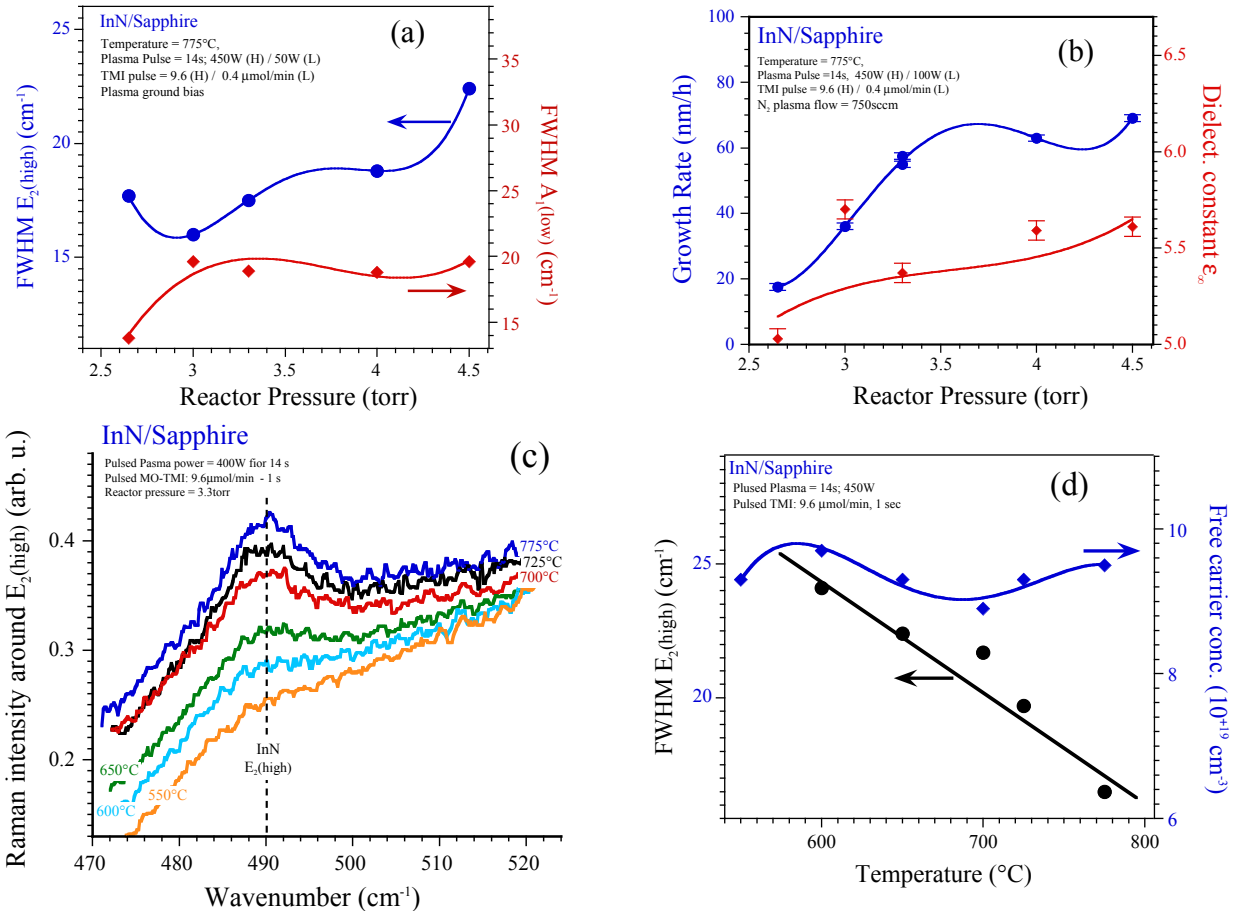

Fig. 4:(a) Influence of reactor pressure of local structural ordering via Raman E_2(high) FWHM; **(b)** Change of growth rate and effective Dielectric function with reactor pressure;**(c)** Evolving of InN E_2(high) mode as function of growth temperature with FWHM values and Free carrier concentrations given in **(d).**

The substrate growth temperature window was assessed from 550°C up to 800°C, using a 14 sec pulsed Plasma exposure and 1 sec TMI pulse exposure. As depicted in Fig. 4 (c) and (d), the Raman E_2(high) mode appears above 650°C and improves significantly with higher growth temperature. Above 800°C, the FWHM values of the E_2(high) mode increase again. The substrate growth temperature window was assessed from 550°C up to 800°C, using a 14 sec pulsed Plasma exposure and 1 sec TMI pulse exposure. As depicted in Fig. 4 (c) and (d), the Raman E_2(high) mode appears above 650°C and improves significantly with higher growth temperature. Above 800°C, the FWHM values of the E_2(high) mode increase again. As shown in Fig. **4(d)**, even though the FWHM of the E_2(high) Raman decreased with increased temperature, the free carrier concentration in the layers remained high, suggesting that other process parameter play a critical role in the high free carrier concentration determined.

3.3. Influence of Plasma power on InN layer properties

The influence of the plasma power plays a critical role on the type and number density of plasma activated nitrogen precursor fragments generated and their kinetic energies in the afterglow regime above and at the growth surface. The structural and optical properties of InN layer are depicted in Fig. 5 as function of plasma power. Fig. 5(a) shows an improvement of the local ordering with an decrease of the E_2(high) FWHM values for plasma powers up to 450 Watts. Above 450 W, the kinetic energy of the ions becomes too high and the growth rate - shown in Fig, 5(b) – decreases, while the FWHM of the E_2(high) mode increases. The free carrier concentration and mobility – depicted in Fig. 5(c) – show a local optimum around 400 – 450W, with no significant changes in growth rate and effective dielectric function.

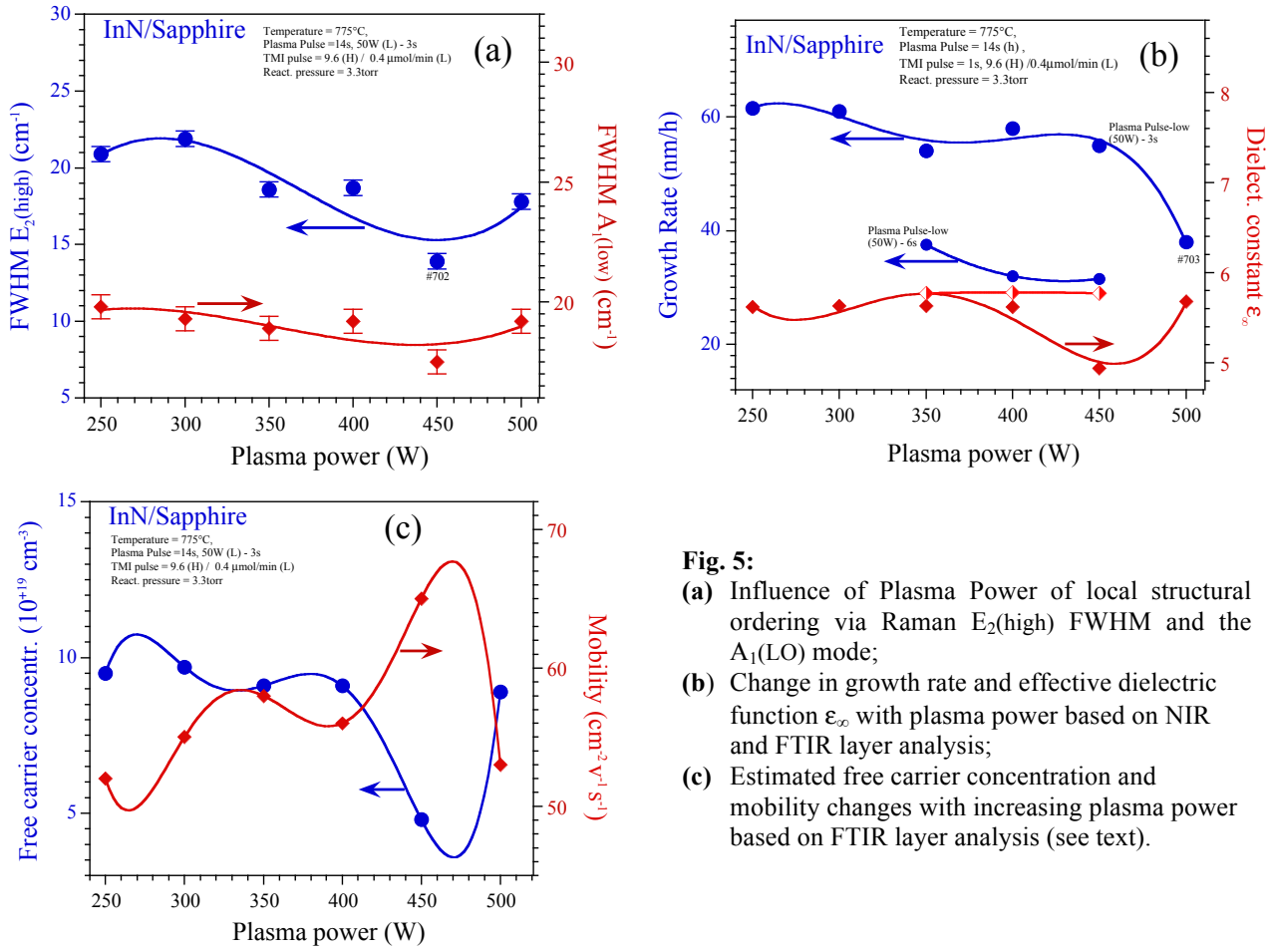

Fig. 5:
(a) Influence of Plasma Power of local structural ordering via Raman E_2(high) FWHM and the A_1(LO) mode;
(b) Change in growth rate and effective dielectric function ε_∞ with plasma power based on NIR and FTIR layer analysis;
(c) Estimated free carrier concentration and mobility changes with increasing plasma power based on FTIR layer analysis (see text).

3.4. Effect of MO-Plasma separation on InN layer properties

In the following Fig. 6, we evaluated the influence of the TMI MO position relative to the start/stops point of the plasma exposure and the exposure length. The MO pulse length was kept constant at 1 sec, with an estimated In-surface coverage of 1 to 1.5 monolayers (ML) per pulsing cycle. The starting of the Plasma pulse has been varied from 3 to 7 sec as depicted in Fig. 6(a) and (b), while the Plasma exposure length was kept at 14 sec at 450 W. The growth rate results indicate a TMI-plasma pulse separation of about 5 sec, while to local ordering data are best around 3 sec and 6 sec. The most pronounced changes are related to the plasma exposure length, which drop significant with exposure length as shown in Fig. 6(c).

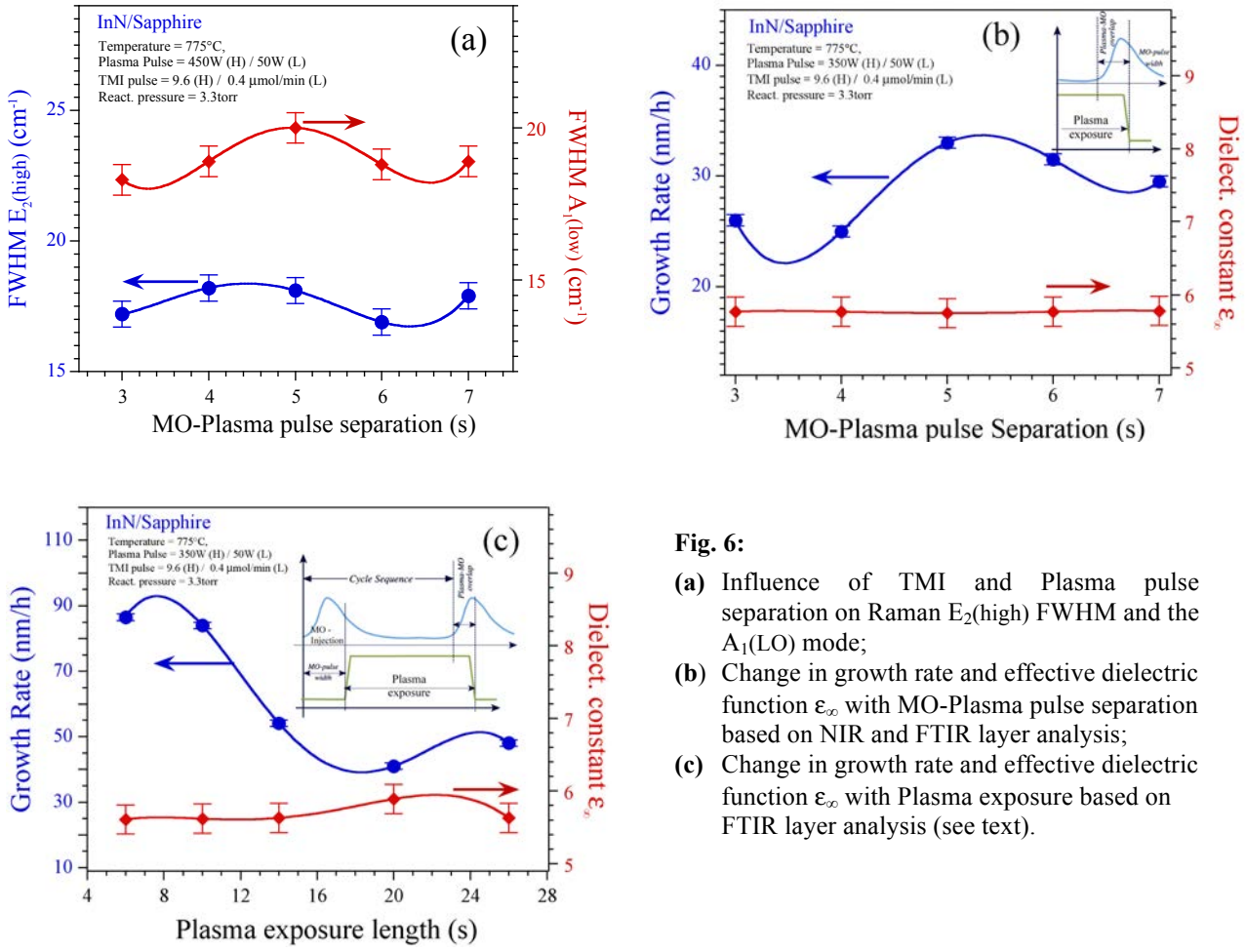

Fig. 6:

(a) Influence of TMI and Plasma pulse separation on Raman E_2(high) FWHM and the A_1(LO) mode;

(b) Change in growth rate and effective dielectric function ε_∞ with MO-Plasma pulse separation based on NIR and FTIR layer analysis;

(c) Change in growth rate and effective dielectric function ε_∞ with Plasma exposure based on FTIR layer analysis (see text).

3.5. Preliminary InGaN results

First $In_{1-x}Ga_xN$ epilayers where deposited on sapphire substrates, using the same process parameter as established of InN layers described above. The MO and plasma exposure times where 1.5 sec and 14 sec, respectively. The TMI and TMG MO precursors where injected simultaneously with TMG/(TMI+TMG) ratio set to achieve a targeted gallium composition x in $In_{1-x}Ga_xN$. The growth temperature was kept constant at 775°C as established for InN. Fig. 7 depicts the Raman spectra in the E_2(high) and A_1(LO) region for x=[0, 0.1, 0.15, 0.2, 0.4 and 0.6], showing a systematic shift and a pronounced a broadening of the A_1(LO) Raman mode as function of composition x[18,19]. For compositions ($0.35 < x < 0.65$) two board A_1(LO) Raman peaks can be distinct, indicating nanoscale phase segregations within the layers.

The representative surface topography of the $In_{0.8}Ga_{0.2}N$ layer is depicted in Fig. 8. As shown in Fig. 8(a), (c) and (d) together with a near-field image Fig. 8(b) acquired using a scattering scanning near-field optical microscope (s-SNOM) [20] with a excitation wavelength of $\lambda = 10.5$ µm. The topography of the sample surface reveals a uniform distribution of island heights throughout the growth area with an average surface RMS of below 2nm. The s-SNOMS near-field amplitude image shows islands with larger permittivity compared to the underlying substrate suggesting a strong phase separation due to the spinodal and binodal decomposition[21] at the growth surface. Further spectroscopic resolved s-SNOM analysis is in progress to relate to lateral composition fluctuations with process parameter.

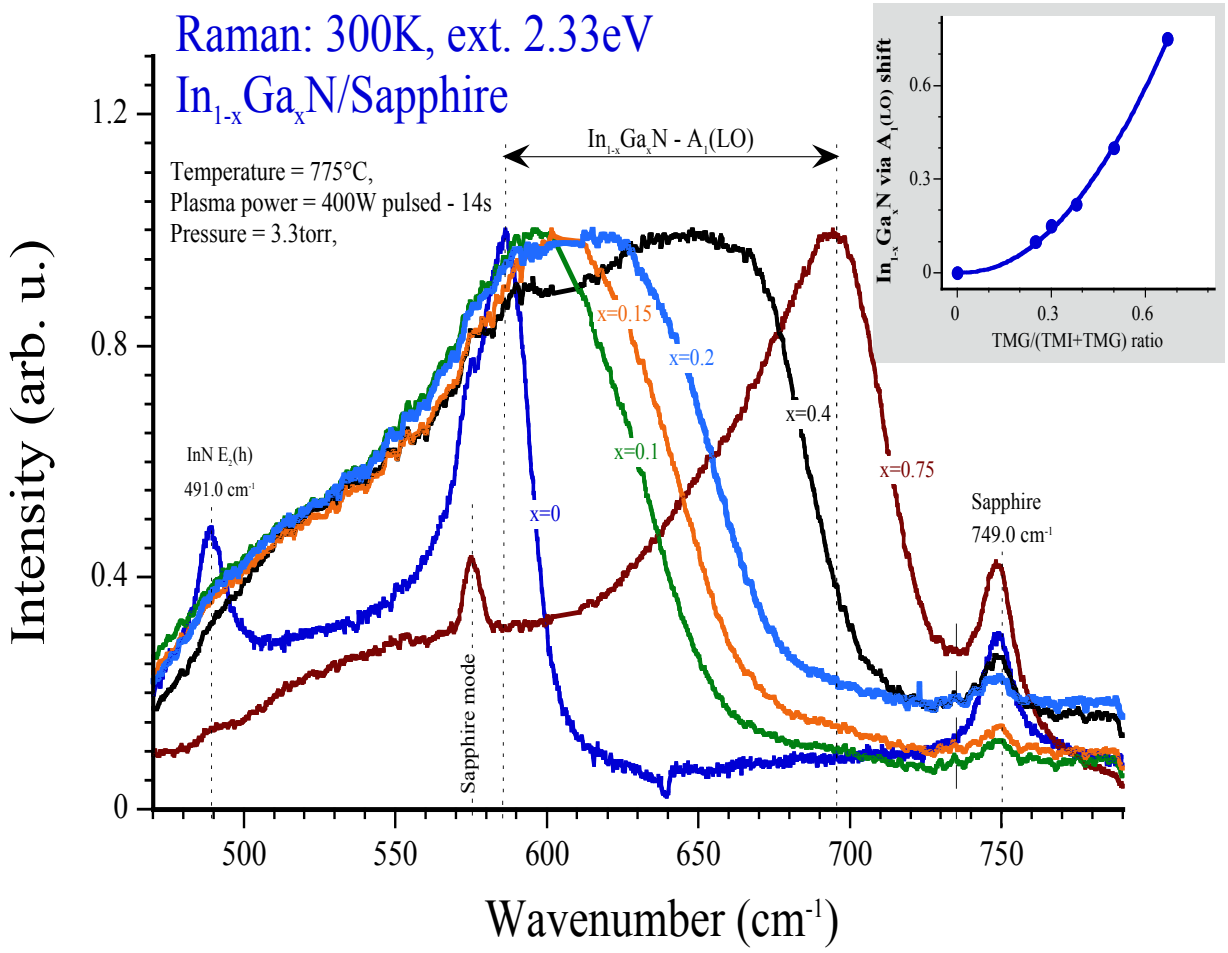

Fig. 7: Shift of $A_1(LO)$ Raman mode with Gallium incorporation in $In_{1-x}Ga_xN$ layers grown on sapphire substrates. The inset displays the estimated Ga composition x via $A_1(LO)$ versus precursor ratio.

4. CONCLUSIONS

In conclusion, we reported first results on $In_{1-x}Ga_xN$ growth by migration-enhanced, plasma-assisted MOCVD, using the afterglow regime of an oxygen-free, hollow cathode nitrogen plasma source. An initial set of an extended process parameter space for InN growth was explored and established an InN growth window of around 775°C, using pulsed MO and nitrogen precursor supply. The InN layers have good local ordering (Raman E_2(high) mode) with free carrier concentration in the 1E+18 to 1E19 range. Indium-rich $In_{1-x}Ga_xN$ layers deposited in the same growth window exhibit lateral compositional fluctuations at the growth surface - as revealed by s-SNOM. These lateral compositional fluctuations lead to nanoscale phase separations in the bulk materials. To which extend such compositional fluctuation at the growth surface can be suppressed through the expanded process parameter space by MEPA-MOCVD will be subject for further studies.

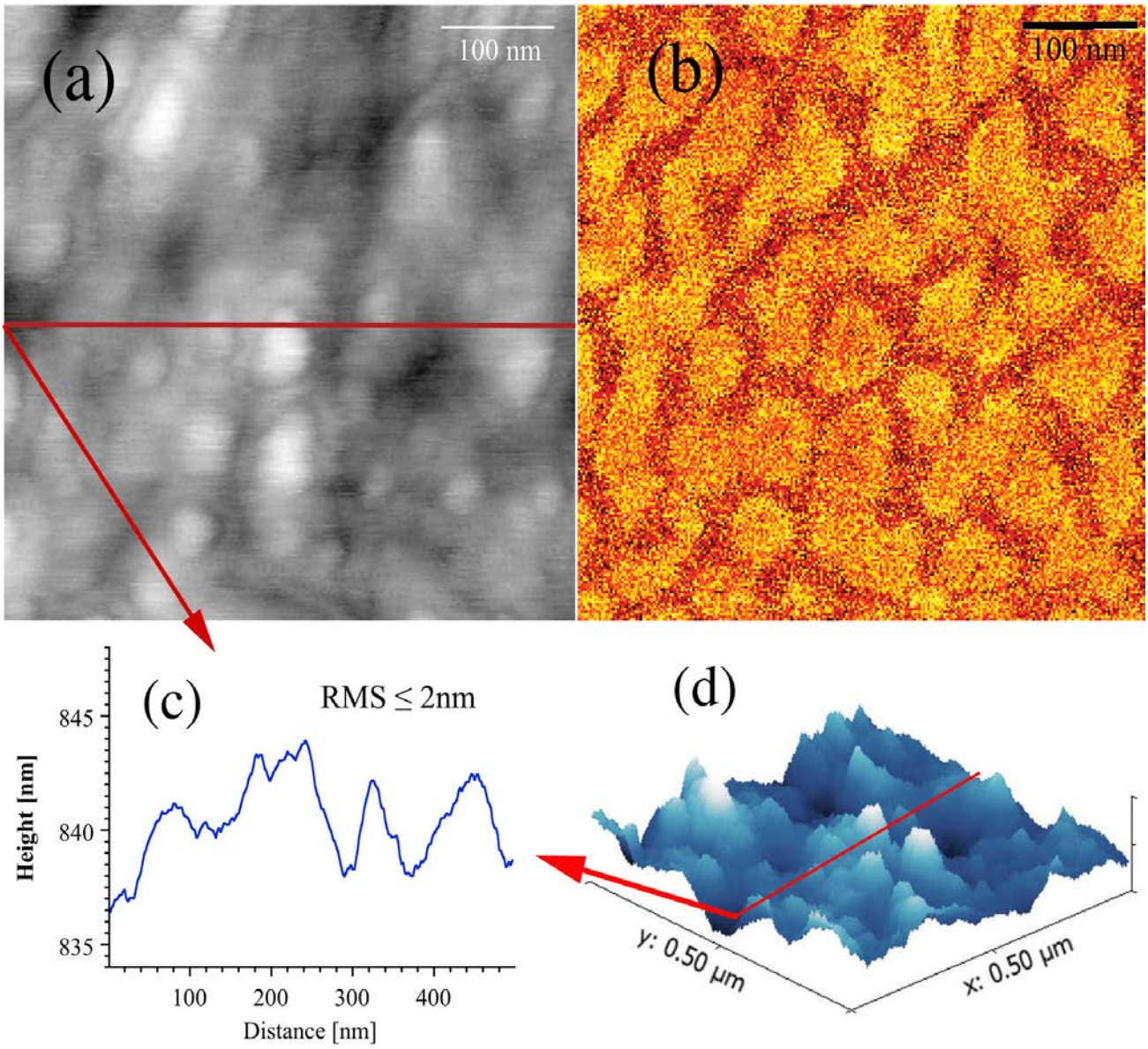

Fig. 8:(a) AFM surface topographic image recorded in tapping-mode for a $In_{0.8}Ga_{0.2}N$ layer with **(c)** a AFM height profile and **(d)** a 3D-contour plot of the 500x500 nm^2 scan area;
(b) s-SNOM image recorded for an excitation wavelength of $\lambda = 10.5$ µm reveals nano-scale compositional fluctuations at the $In_{0.8}Ga_{0.2}N$ growth surface (see text).

5. ACKNOWLEDGEMENT

This work was supported by the AFOSR grant # FA 9550-10-1-0097 and GSU-RPE.

REFERENCES

[1] N. Miller, E. E. Haller, G. Koblmüller, C. Gallinat, J. S. Speck, W. J. Schaff, M. E. Hawkridge, K. M. Yu and J. W. Ager, Phys. Rev. B 84(7), p.075315 (2011).

[2] X. Wang, S. Liu, N. Ma, L. Feng, G. Chen, F. Xu, N. Tang, S. Huang, K. J. Chen, S. Zhou and B. Shen, Appl. Phys. Express 5, p.015502 (2012).

[3] N. A. Masyukov and A. V. Dmitriev, J. Appl. Phys. 109, 023706 (2011).

[4] S. S. Khludkov, I. A. Prudaev, and O. P. Tolbanov, Russ. Phys. J. 56(9), pp.997-1006 (2014).

[5] Ian M. Watson, Coordination Chemistry Reviews 257(13–14), pp.2120-2141 (2013).

[6] D. A. Browne, B. Mazumder, Y.-R. Wu and J. S. Speck, J. Appl. Phys. 117, p.185703 (2015).

[7] Z. Mi and S. Zhao, physica status solidi (b) 252(5) pp.1050-1062 (2015).

[8] S. Valdueza-Felip, E. Bellet-Amalric, A. Núñez-Cascajero, Y. Wang, M.-P. Chauvat, P. Ruterana, S. Pouget, K. Lorenz, E. Alves and E. Monroy, J. Appl. Phys. 116, 233504 (2014).

[9] N. Hong Tran, B. Huy Le, S. Fan, S. Zhao, Z. Mi, B. A. Schmidt, M. Savard, G. Gervais and K. S. A. Butcher, Appl. Phys. Lett. 103, 262101 (2013).

[10] G. B. Stringfellow, J. Cryst. Growth 312(6), pp.735-749 (2010); http://dx.doi.org/10.1016/j.jcrysgro.2009.12.018

[11] "Indium-nitride growth by HPCVD: Real-time and ex-situ characterization," N. Dietz, book chapter 6 in "III-Nitrides Semiconductor Materials", ed. Z.C. Feng, Imperial College Press, pp. 203-235 (2006).

[12] M. Buegler, M. Alevli, R. Atalay, G. Durkaya, I. Senevirathna, M. Jamil, I. Ferguson, and N. Dietz, Proc. SPIE Vol. **7422** p. 742218 (2009).

[13] M. Buegler, S. Gamage, R. Atalay, J. Wang, I. Senevirathna, R. Kirste, T. Xu, M. Jamil, I. Ferguson, J. Tweedie, R. Collazo, A. Hoffmann, Z. Sitar, and N. Dietz, Proc. of SPIE Vol. **7784**, paper# 77840F-1-7 (2010).

[14] Kenneth Scott A. Butcher, Dimiter Alexandrov, Penka Terziyska, Vasil Georgiev, Dimka Georgieva, and Peter W. Binsted, physica status solidi (a) **209**(1), 41-44 (2012).

[15] M. K. I. Senevirathna, S. Gamage, R. Atalay, A. R. Acharya, A. G. U. Perera, N. Dietz, M. Buegler, A. Hoffmann, L. Su, A. Melton, and I. Ferguson, J. Vac. Sci. Technol. A **30**(3), pp.031511-6 (2012).

[16] A. B. Weerasekara, Z. G. Hu, N. Dietz, A. G. U. Perera, A. Asghar, M. H. Kane, M. Strassburg, and I. T. Ferguson, J. Vac. Sci. Technol. B **26**(1), pp. 52-55 (2008).

[17] N. Dietz, "Real-time optical Characterization of thin film growth," Mater. Sci. & Eng. B87(1), pp.1 - 22 (2001).

[18] S. Hernandez, R. Cusco, D. Pastor, L. Artus, K. P. O'Donnell, R. W. Martin, I. M. Watson, Y. Nanishi, and E. Calleja, J. Appl. Phys. 98(1) pp.).

[19] R. Oliva, J. Ibáñez, R. Cuscó, R. Kudrawiec, J. Serafinczuk, O. Martínez, J. Jiménez, M. Henini, C. Boney, A. Bensaoula, and L. Artús, J. Appl. Phys. **111**(6), p. 063502 (2012).

[20] S. Mastel, S. E. Grefe, G. B. Cross, A. Taber, S. Dhuey, S. Cabrini, P. J. Schuck and Y. Abate, Appl. Phys. Lett. **101**, p.131102 (2012).

[21] C. Tessarek, S. Figge, T. Aschenbrenner, S. Bley, A. Rosenauer, M. Seyfried, J. Kalden, K. Sebald, J. Gutowski and D. Hommel, Phys. Rev. B **83**, p.115316 (2011).